

# **PROJECT UX-1353: GEM-3D (SEED)**

## **FINAL REPORT**

rev. 1

30 April 2004

### **LEAD PERFORMER:**

Dr. Kevin O'Neill  
USACoE ERDC-CRREL  
72 Lyme Rd  
Hanover NH 03755  
koneill@CRREL.usace.army.mil

### **Co-PI:**

Dr. I.J. Won  
Geophex Ltd  
605 Mercury St  
Raleigh NC 27603  
Ph: 919-839-8515  
ijwon@geophex.com

<b>REPORT DOCUMENTATION PAGE</b>				<i>Form Approved OMB No. 0704-0188</i>	
<small>The public reporting burden for this collection of information is estimated to average 1 hour per response, including the time for reviewing instructions, searching existing data sources, gathering and maintaining the data needed, and completing and reviewing the collection of information. Send comments regarding this burden estimate or any other aspect of this collection of information, including suggestions for reducing the burden, to the Department of Defense, Executive Services and Communications Directorate (0704-0188). Respondents should be aware that notwithstanding any other provision of law, no person shall be subject to any penalty for failing to comply with a collection of information if it does not display a currently valid OMB control number.</small>					
<b>PLEASE DO NOT RETURN YOUR FORM TO THE ABOVE ORGANIZATION.</b>					
<b>1. REPORT DATE (DD-MM-YYYY)</b>		<b>2. REPORT TYPE</b>		<b>3. DATES COVERED (From - To)</b>	
<b>4. TITLE AND SUBTITLE</b>				<b>5a. CONTRACT NUMBER</b>	
				<b>5b. GRANT NUMBER</b>	
				<b>5c. PROGRAM ELEMENT NUMBER</b>	
<b>6. AUTHOR(S)</b>				<b>5d. PROJECT NUMBER</b>	
				<b>5e. TASK NUMBER</b>	
				<b>5f. WORK UNIT NUMBER</b>	
<b>7. PERFORMING ORGANIZATION NAME(S) AND ADDRESS(ES)</b>				<b>8. PERFORMING ORGANIZATION REPORT NUMBER</b>	
<b>9. SPONSORING/MONITORING AGENCY NAME(S) AND ADDRESS(ES)</b>				<b>10. SPONSOR/MONITOR'S ACRONYM(S)</b>	
				<b>11. SPONSOR/MONITOR'S REPORT NUMBER(S)</b>	
<b>12. DISTRIBUTION/AVAILABILITY STATEMENT</b>					
<b>13. SUPPLEMENTARY NOTES</b>					
<b>14. ABSTRACT</b>					
<b>15. SUBJECT TERMS</b>					
<b>16. SECURITY CLASSIFICATION OF:</b>			<b>17. LIMITATION OF ABSTRACT</b>	<b>18. NUMBER OF PAGES</b>	<b>19a. NAME OF RESPONSIBLE PERSON</b>
a. REPORT	b. ABSTRACT	c. THIS PAGE			<b>19b. TELEPHONE NUMBER (Include area code)</b>

This report was prepared under contract to the Department of Defense Strategic Environmental Research and Development Program (SERDP). The publication of this report does not indicate endorsement by the Department of Defense, nor should the contents be construed as reflecting the official policy or position of the Department of Defense. Reference herein to any specific commercial product, process, or service by trade name, trademark, manufacturer, or otherwise, does not necessarily constitute or imply its endorsement, recommendation, or favoring by the Department of Defense.

## THE GEM-3D

1. Executive Summary .....	5
2. Objective .....	6
3. Background .....	7
3.1 Overall .....	7
3.2 Some Specific Motivation .....	10
4. Materials and Methods .....	18
5. Results and Accomplishments.....	24
References .....	30

## ACKNOWLEDGMENT

The work reported here on design, development, and testing of the GEM-3D instrument was supported by the Strategic Environmental Research and Development Program, under project # UX-1353. The principal investigator was Dr. Kevin O'Neill from the U.S. Army Corps of Engineers, Engineer Research and Development Center (ERDC), Hanover Site. Mr. Byron Young ably assisted him in much measurement and data handling work. The ERDC personnel worked closely with the instrument developers at Geophex Ltd, who performed the heart of the work. Under Dr. I.J. Won and Mr. Alex Oren, technical work at Geophex was carried out by Bill Sanfillipo and Frank Funak, with admirable persistence, insight, and ultimately success.

## LIST OF FIGURES

Figure 1. Concentric coil arrangement of existing GEM-3 design, showing Tx coil currents (arrows). The main transmitting coil is outermost, and the bucking coil with counter-circulating current is inside it, largely nullifying the primary field over the area of the innermost receiving coil. ....	7
Figure 2. General representation of received time domain signal (R) vs log of time. ....	9
Figure 3. Left: Mortar (bottom) and machined steel prolate spheroid with similar proportions; Right: Other machined steel and aluminum targets, used singly or in combination to compete with the UXO. ....	11
Figure 4. Measure of mismatch (vertical axis) for each target or combination of targets, relative to the UXO. ....	13
Figure 5. Test setup, showing measurement surfaces for identifying model parameters and also for testing the signal predictions they produce. ....	14
Figure 6. Top: Good agreement between "actual" $H_z$ (here: horizontal fields) computed over the Testing Area and those obtained from the SEA using the $S_{j,k}$ inferred from vector data over the PID surfaces. Bottom: Poor agreement for the same, using only scalar ( $H_z$ ) data on the BC surfaces to obtain the $S_{j,k}$ . ....	16
Figure 7. Synthetic compound object from which a known signal can be produced for use in the ill-conditioning evaluation. ....	17
Figure 8. Condition numbers of the matrices from the four different survey methods, relative to that for the first one. ....	18
Figure 9. Schematic of GEM-3D and UXO with the magnetic field lines produced by each. ....	19
Figure 10. Contours of the logarithm of transmitted magnetic field magnitude for a GEM-3 type coil configuration. Blue = low, red = high. Horizontal axis runs across the surface of the sensor head; vertical axis is normal to it, axis units are meters. Red concentrations on the horizontal axis surround the two sets of transmitter loop wires. ....	19
Figure 11. The GEM-3D sensor head. ....	20
Figure 12. Left: Schematic of the laser positioning system concept, with three receivers located on the plane of the Tx coils of the EM sensor head. Right: An early realization of the system, with tube shaped amplifiers also attached to each laser receiver. ....	23
Figure 13. Most current application of the system, similar to the concept in Figure 12, right, but with the plane of laser receivers and amplifiers displaced about 30 cm above the sensor head, on styrofoam. ....	23
Figure 14. GEM-3D data along measurement lines in a plane over a vertical UXO. ....	24
Figure 15. GEM-3D measurements at 510 Hz (quadrature component) over a plane above a UXO in vertical orientation (top row) and horizontal orientation (bottom row). component, i.e. in direction aligned with the axis of the UXO when it is horizontal. ...	25
Figure 16. Some more machined test objects to round out the prolate spheroid selection. ....	26
Figure 17. Comparison of GEM-3D measurements of $H_z$ for an AL prolate spheroid. ....	27
Figure 18. Comparison of GEM-3D measurements of $H_z$ for a steel prolate spheroid. ....	27

## TABLES

Table 1. Objects and combinations of objects used with the UXO in pattern recognition discrimination exercise. ....	12
---	----

## **ACRONYMS and ABBREVIATIONS**

A/D: Analog to digital (converter, signal processor)

DSP: Digital signal processor

EMI: Electromagnetic induction

ESTCP: Environmental Security Technology Certification Program

FD: Frequency domain

GEM-3: Geophex Geophysical Electromagnetic Induction survey instrument, model 3.

GEM-3D: GEM-3 with vector receiver, developed under the project reported here.

GEM-3DL: GEM-3D with laser positioning

(k)Hz : (kilo)Hertz, 1 Hertz = 1 cycle per second (frequency)

SEA: Standardized Excitations Approach

SERDP: Strategic Environmental Research and Development Program

TD: Time domain

USB: Universal serial bus

UWB: Ultra-wideband

UXO: Unexploded ordnance

WinGEM: Software to operate the GEM-3, GEM-3D, and GEM-3DL using a PC with MS  
Windows OS.

# 1. Executive Summary

The objective of this project was to construct, debug, and demonstrate, at the bench and "backyard" level, a new frequency domain (FD) UWB electromagnetic induction (EMI) sensor configuration designated here as the GEM-3D. The driving force behind design and development of this instrument is the need for improved unexploded ordnance (UXO) discrimination. In this regard, the details of our motivation for producing this device suggest the advantages that may be obtained from it: A new, more complete EMI signature system for UXO and other metallic objects appears to benefit from processing that employs complete vector signal information. The configuration of the existing Geophex GEM-3 was used as a starting point for the new device, the essential difference being that the new instrument would receive and record separately three orthogonal magnetic field components instead of one. This was accomplished by adding two receiver coils that are the same size as the original single coil but which are perpendicular to it and to each other. This completely defines the vector field that constitutes the EMI response of an object of interest. The instrument has an expanded bandwidth relative to established versions of the GEM-3, going from the same lower limit of  $\sim 30$  Hz up to at least  $\sim 50$  kHz, with a maximum of about 15 frequencies recordable in each channel, i.e. for each orthogonal signal component (using slightly fewer is recommended). The new sensor is handheld, and therefore capable of being swept and tilted in any direction, generating arbitrary angles of excitation and reception ("views"). This motivated integration of flexible, high accuracy positioning, which was done under other (non-SERDP) auspices. The laser positioning system that was implemented is capable of sub-millimeter accuracy, and was configured to provide all tilt angles in a version of the instrument dubbed the GEM-3DL. Except where noted otherwise, the material in this report concentrates on the SERDP-supported GEM-3D.

The bench version of the instrument that was achieved appears to work well by both quantitative and qualitative criteria. Proper (and illuminating) symmetries and asymmetries appear in the different received field components as the sensor head is swept over UXO's and other objects. Measured data for machined spheroids of different materials and shapes compare very well to corresponding analytical solutions that account for the details of the GEM's transmitted ("primary") field. In upcoming years, pending further support, we plan to streamline and harden the instrument, particularly in connection with the laser positioning system; to apply it in backyard and field tests; and to demonstrate the UXO discrimination advantages that may be obtained.

## 2. Objective

This work responded to SERDP SON UXSEED-03-01, Exploratory Development Program (Seed) Son For Fy03, dated Nov 14, 2001: Innovative Approaches To Unexploded Ordnance (UXO) Cleanup. The objective was to construct, debug, and demonstrate, at the bench and "backyard" level, a new frequency domain (FD) UWB electromagnetic induction (EMI) sensor configuration designated as the GEM-3D. As in the existing GEM-3, when the sensor head is horizontal, it is to be capable of measuring vertical magnetic secondary magnetic fields, i.e. the scattered fields from a metallic object that constitute the EMI signal. This design was to be modified so as to record horizontal secondary field components as well. This was done using the existing Geopex GEM-3 design as a basis, with an expanded bandwidth (up to at least  $\sim 50$  kHz). The sensor was to be handheld, and therefore capable of being tilted in any direction, generating arbitrary angles of excitation and reception ("views"). Thus, while the three orthogonal receiver coils do not always correspond to "vertical" and "horizontal," they still always provide the full vector definition of the secondary field (signal). This flexibility would be a liability without sophisticated positioning system. Therefore further development of the device was also undertaken, under ERDC auspices, integrating laser positioning into it. With that addition it is designated as the GEM-3DL. This report will concentrate on the SERDP-supported GEM-3D; where designated, material on the GEM-3DL and other lines of development from the original concept are presented as well.

The intention of this work was to proceed by constructing an instrument with a GEM-3-like concentric coil arrangement for the horizontal coils, including two transmitter and one receiver coils, as shown in Figure 1. Two orthogonal vertical receiving coils (with perpendicular, horizontal axes) were to be added, with their centers at the common mid-point of the horizontal coils. The device was to have the same advantages in spatial and frequency resolution as the newest GEM-3. Some indication was also to be produced, suggesting the utility of the additional diversity for UXO discrimination. Overall, the driving motivation for this work was to produce a device that would facilitate superior UXO detection and discrimination. The instrument should function at least as well as the older GEM-3 series in detection, with horizontal components enhancing direction indications of target locations. However we did not seek to optimize design for anomaly detection but instead aimed for providing a better basis for discrimination of UXO's from other arbitrary metallic geometries (clutter).



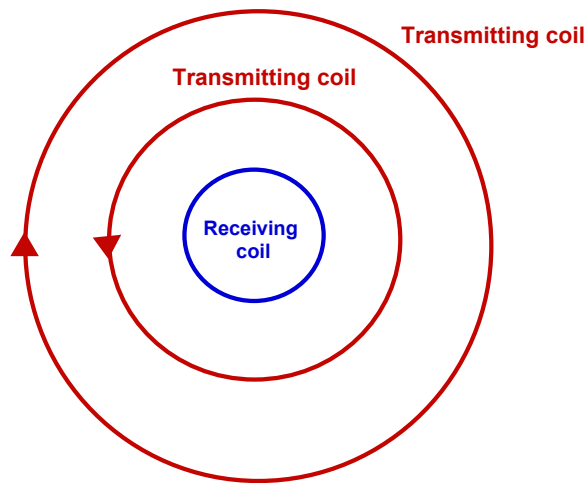


Figure 1. Concentric coil arrangement of existing GEM-3 design, showing Tx coil currents (arrows). The main transmitting coil is outermost, and the bucking coil with counter-circulating current is inside it, largely nullifying the primary field over the area of the innermost receiving coil.

## 3. Background

### 3.1 Overview

Detection and especially discrimination of buried unexploded ordnance (UXO) from omnipresent metallic clutter is a persistent, expensive, and pressing problem. While it is not yet clear whether or which other technologies might be best used in conjunction with electromagnetic induction (EMI) for UXO discrimination, it is clear that EMI is currently a front runner in the development of new, more effective approaches. Virtually all EMI sensors transmit a "primary" field and receive signals ("secondary" field) using wire coil antennas. Frequency domain (FD) EMI systems use such coils to transmit (Tx) a "primary" magnetic field with selection of frequencies over a chosen band – possibly only a single frequency - simultaneously receiving (Rx) and recording

responses to those frequencies (the "secondary" field). Thus a central problem in frequency domain sensors is the isolation of the receiving coils from the primary field, the latter being very large relative to the secondary field, particularly when the receivers are near the transmitters, as contemplated here. Physical separation of the Tx and Rx coils is a possible approach. However this typically degrades spatial resolution and handy manipulation of the instrument. Therefore, remaining with co-located Tx and Rx coils, we implement a "bucking" coil, which transmits a field that opposes the primary field at the location of the receiving coil. By canceling out the primary field at the receiver as much as possible, one is left (ideally) with only the secondary field from the target. Other approaches are possible for finding the secondary field amidst the much stronger primary field, e.g. using differencing schemes between stacked or symmetrically distributed coils, but the fundamental problem is the same.

The "bucking" discussion above is particularly pertinent when one attempts 3-D vector definition of the secondary field. The geometrical arrangement of the main and the bucking coils is crucial to successful suppression of the primary field at the receiver. However, to our knowledge no FD EMI instruments have been produced to date that are capable of suppressing the primary field in one receiver orientation while also suppressing it in other directions as well. Most imaginable arrangements of two bucking coils that work well for one receiver orientation would in fact exacerbate the problem for other receiver orientations. This observation would appear to favor the development of time domain (TD) systems for obtaining vector EMI response. Most TD systems operate by transmitting a steady signal, saturating a metal object of interest, then shutting the transmitter off. A receiver then records the secondary field from the object as that field decays in response to the sudden shut off. The receiver only operates while the transmitter is off, thereby dodging the primary field. While this bypasses the bucking problem, a number of things motivate us to proceed in the FD: FD systems claim the advantage in having superior control of selection and power in the frequency content of data produced, and thus in the equivalent time domain signal, which can readily be obtained from the FD data. In practice, FD systems are less band limited than TD systems and can therefore offer a *greater* equivalent time range of response than the actual TD systems. Consider Figure 2 below.

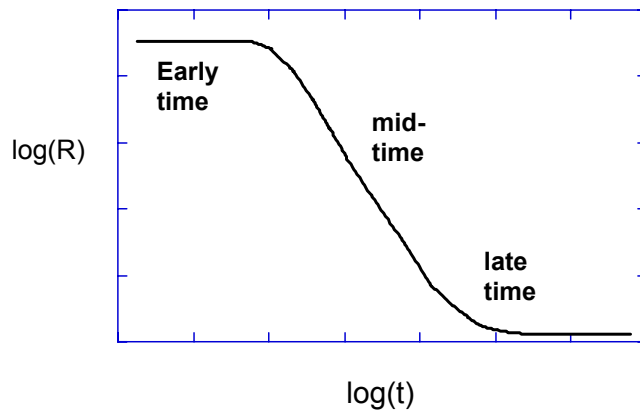


Figure 2. General representation of received time domain signal (R) vs log of time.

While there has been progress in "very early time" EMI devices, in general TD devices are unable to shut off the transmitter and damp the effects of the transition quickly enough to get very early time data. Information in such data is the equivalent of high frequency FD data. The latter is of strong interest because it provides information on asymptotic limits of scattering behavior: The induced currents penetrate the target negligibly and the secondary fields they produce do not depend on the type of metal encountered. This may offer hope of avoiding very substantial complications in UXO discrimination, given that many if not most UXO are composites of different metals. At the other end of the spectrum, TD signals naturally fade as the target's responses wind down. This means that very late time data is unlikely to be detectable above the noise. Thus the equivalent of low frequency asymptotic limits will be poorly defined or absent. While FD systems must also struggle with some challenges in the equivalent very low frequency range, on the whole it is much more feasible to get data from them in that part of the EMI band. Many UXO produce significant response patterns in the 10's of Hz. Low frequency asymptotic limits and fundamental signal features containing basic target shape information appear in many cases only well below 30 Hz [SERDP Project 1122, Final Report]. To get at the TD equivalent of these frequencies using TD instruments would require recording out to the order of tenths of a second. Highly unlikely. At least at the research level, FD EMI measurements have been made successfully over a continuous UWB ranging from a few Hz up to about 300 kHz, roughly the TD equivalent of spanning times from a micro-seconds to tenths of a second. Recent work by Geophex on TD systems in a GEM configuration may be an exception to the limitations cited above, and we look forward to encountering that new device.

All things considered, we proceeded here with a FD system, using the methods described in Section 4 to dodge the primary field.

### **3.2 Some Specific Motivation**

Why map full vector EMI response over some region of space, e.g. a volume above a target? Or, if one is going to map response with high data density over some region, isn't a single field component sufficient to define what we need? Are the others just redundant? Do we benefit from the right kind of "redundancy"? Our recent research has shown that, with sufficient data, we can construct a new generation of forward models for UXO or other objects, including all near and far field effects, geometrical and material heterogeneity, and internal interactions. These are not fine points. Other established models fall down, to different degrees in different circumstances, as a result of the factors cited. Appendix I was composed as a white paper for the SERDP/ESTCP EMI Workshop in Annapolis, 3-4 Feb 2004, and will be submitted as a state of the art review shortly. It describes one's EMI modeling options and the features and virtues of the new generation of models, using relatively simple language and mathematics. Basically, depending on the model of UXO EMI response one employs, one might in principle be able to infer target parameters from the more restricted data alone. However here is where theoretical appearance and practical reality diverge. Like most inversion calculation, inference of EMI target parameters from measured signals over a restricted grid or plane is often plagued by ill-conditioning.

Our new signature system formulates an object's response in terms of its reaction to a defined collection of fundamental or standardized excitations (SE). Any arbitrary (actual) primary field can be decomposed into these basic components, which are either mathematical eigenfunctions or fields transmitted by some standardized set of hypothetical equivalent sources. The response of the target to each of these basic stimuli is inferred. The crux of the method lies in the fact that the scattering parameters defining each of these basic responses are characteristics of the object investigated. Once they have been inferred in the course of general inversion, they can be examined for target classification. Alternatively, if inferred under controlled circumstances, they provide a forward scattering model for particular targets that is fast enough for use in either general inversion calculations or, in the least, pattern matching type classification algorithms. For reference in what follows, the expression of a secondary field signal  $\Psi^s$  can be expressed in the SE Approach (SEA) as

$$\Psi^s = \sum_{j=1}^J b_j \sum_{k=1}^K S_{j,k} \Psi_k^s \quad (1)$$

where the  $b_j$  are determined by the primary field under any particular circumstances, each  $b_j$  indicating the strength of participation of the  $j^{\text{th}}$  standardized excitation; and the  $S_{j,k}$  are a set of  $K$  response coefficients corresponding to the  $j^{\text{th}}$  excitation. While this equation is written in terms of a scalar magnetic potential  $\Psi$ , the parameterization for an equation in terms of the vector magnetic field  $\mathbf{H}$  is the same. One simply replaces  $\Psi^s$  by  $\mathbf{H}^s$  and  $\Psi_k^s$  by  $(-\nabla \Psi_k^s)$ .

The capabilities of the method for representing the rather problematical UXO in Figure 3 are shown in Appendix I, where the forward solution performance of the SEA is compared to that from the next most complete system [3]. Here we demonstrate the use of the method in inversion with the following example, in which we wish to distinguish the UXO from other metallic objects among those in the figure.



Figure 3. Left: Mortar (bottom) and machined steel prolate spheroid with similar proportions; Right: Other machined steel and aluminum targets, used singly or in combination to compete with the UXO.

The particular set of objects chosen for measurements, including some combinations of them, are listed in the table below.

**Table 1.** Objects and combinations of objects used with the UXO in pattern recognition discrimination exercise.

Object	Material	axis(2a)	axis(2b)	elongation (e)
S2	Steel	30mm	182mm	6
S3	Steel	30mm	90mm	3
S4	Steel	15mm	90mm	6
S7	Steel	30mm	30mm	1
A2	Aluminum	30mm	91mm	3
A3	Aluminum	15mm	91mm	6
C1	S4; S7			
C2	A3; S7			
U1	UXO made of mainly steel			

By sweeping the GEM-3 sensor above each of these objects in various orientations we are able to infer  $S_{j,k}$ , knowing what primary field the instrument produces. That is, knowing  $b_j$  and measuring the equivalent of  $\Psi^s$  in (1), we can solve for the essential, characteristic response coefficients. To classify each object relative to the UXO we optimize the match between the  $S_{j,k}$  obtained from a particular set of measurements and those we have already established for the UXO. Figure 4 shows a normalized set of residual mismatches from the processing for each target or combination thereof, relative to the expected signature of the UXO in terms of the  $S_{j,k}$ . The UXO (U1) provides the best match. That is, when the UXO was placed in a new position relative to the sensor and surveyed as an "unknown," the inferred  $S_{j,k}$  best matched those in the library for that UXO, as opposed to those for the other objects. The next closest item has about four times the mismatch magnitude, even though it is also steel and somewhat similar in general proportions (Figure 3, left).

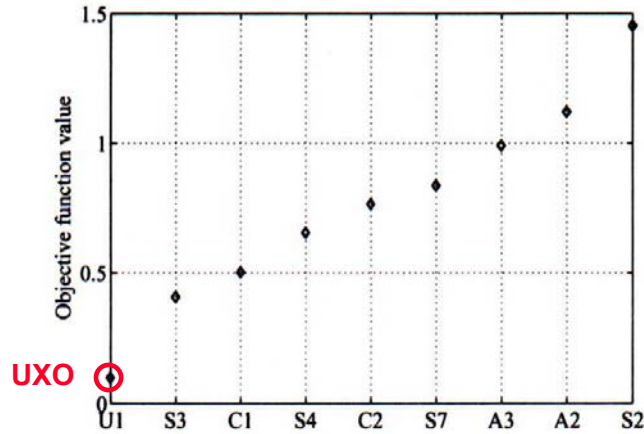


Figure 4. Measure of mismatch (vertical axis) for each target or combination of targets, relative to the UXO.

The implications of the figure can be construed in a couple of ways:

- As an exercise in simple "fingerprinting." It indicates that, if one makes a set of measurements over these objects as unknowns and then simply calculates the best possible match of each set of extracted response coefficients to those of the UXO, the UXO would be identified as such.
- As a reassurance for more general inversion: In this approach we have no library of target signatures but simply blindly extract the response coefficients to feed into some classifier, e.g. SVM trained on various classes of UXO. The figure reflects the fact that all the different objects have response coefficients that are different from one another and all are significantly different from the UXO. This in turn suggests that a properly designed general inversion routine should be able to single out U1, in particular as "UXO-like."

But how difficult is it to obtain these response coefficients? While the results above are inspiring, they will not lead to practical results if extracting the  $S_{j,k}$  from field data is unrealistic. Otherwise put: what is necessary, in terms of data, to extract the  $S_{j,k}$  successfully? In principle, we can always make enough measurements to solve uniquely for or optimize for the  $S_{j,k}$ . However, as mentioned above, ill-conditioning in a system of equations from such measurements is the entrenched enemy of successful parameter extraction. An ill-conditioned matrix is one with a high "condition number," meaning the ratio between the highest and the lowest eigenvalue. The condition number can be large, for example, when one bit of information sought is very weakly present relative to others. While one may be able to bash through a numerical solution of an ill-

conditioned matrix, skating around "algorithmic singularity," the ill-conditioning serves to amplify greatly any (inevitable) error in input.

As a test/illustration of this, we use a rigorous, detailed numerical model [4-6] that has been shown to model successfully the details of EMI scattering from an aluminum-steel-brass compound target (Figure 5, bottom). This detailed model generates data at two measurement levels, which are the parameter identification (PID) surfaces in the figure. Data from these surfaces is used to derive a "reduced" i.e. SEA model, the validity of which is then tested over the uppermost surface ("testing area.") Reduced SEA forward models based on both 1-D (scalar) and 3-D (vector) received data are evaluated. Note that the PID measurement areas are of limited extent relative to the size of the target, as will often be the case in practice. The arcs labeled  $Q_{p,m,i}$  just indicate distributions of equivalent or fictitious sources used in one of the SEA approaches, corresponding to the  $S_{j,k}$  response parameters mentioned above.

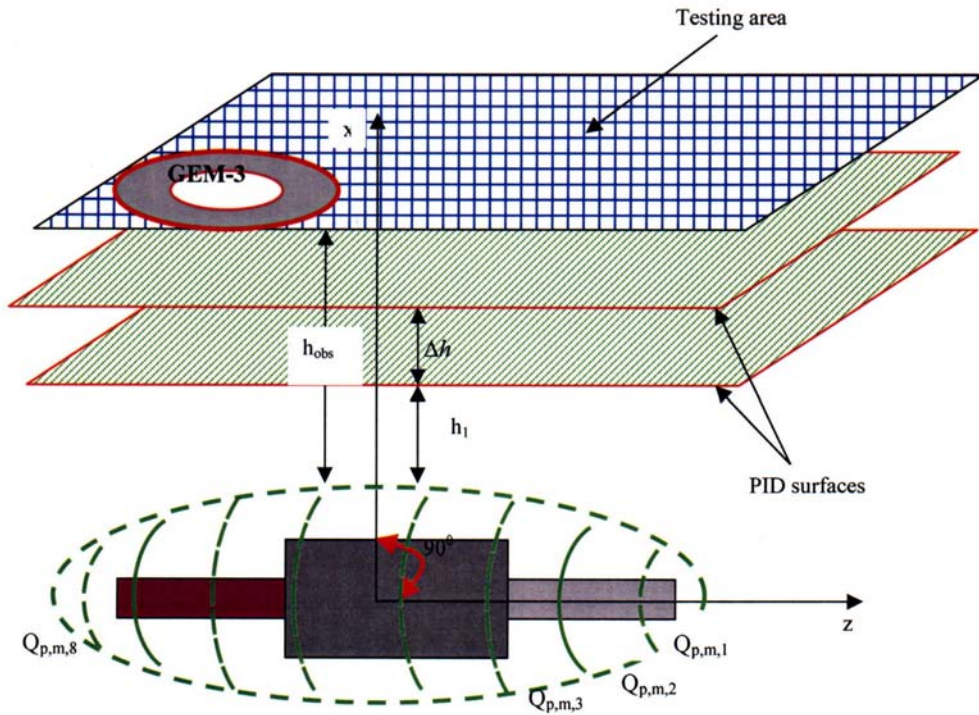


Figure 5. Test setup, showing measurement surfaces for identifying model parameters and also for testing the signal predictions they produce.



Figure 6 shows  $H_z$  values (in this instance, a horizontal component) that would be obtained from sensor sweeps left to right along the line Z-oriented lines on the testing surface. As the sensor sweeps along each line it produces a maximum response at some point closest to the target; thus successive sweeps produce the sequence of peaks seen in the figure. Values obtained from the SEA based only on scalar data from the PID surfaces do not extrapolate well under this change in elevation (Figure 6, bottom). However when the  $S_{j,k}$  for the SEA are obtained from vector PID data, there is excellent agreement between values produced by the reduced sources model and numerical "truth" (Figure 6, top) At least in part because significant secondary fields are only "measured" over a limited extent of PID area, the complete nature of the scattered field is insufficiently represented in the (pseudo) inversion of (1) when only scalar data were exploited. Details are reported in [9].

Pursuing this, we perform another simulation test using the spheroidal eigenfunction based SEA (see [10], which also contains the material leading to Figure 1). The assumed target has two sections, one steel about 1 m long and another non-magnetic material about 30 cm long (Figure 7). Using new analytical solutions [7,8] obtained under other SERDP support, we can calculate the exact expected response from such an object under illumination by the GEM-3, over a 5 by 5 grid of points on measurement surfaces at two different elevations. The target is placed at an arbitrary angle beneath the lower of the two surfaces. In other words, we produce the left side of (1) as data and we can readily calculate the  $b_j$  that are required. Four different survey systems are employed, producing data with:

1.  $H_x$ ,  $H_y$ , and  $H_z$  at two antenna elevations
2.  $H_x$ ,  $H_y$ , and  $H_z$  at one antenna elevation
3.  $H_z$  only, at two antenna elevations
4.  $H_z$  only, at one antenna elevation

Figure 8 shows results in terms of the condition number of the resulting matrices generated under the different survey strategies, as we seek to infer the SEA scattering coefficients. That is, we have divided the condition number of each survey matrix by that of the matrix for the maximum information case #1, with all three vector components measured over two levels. We note that the same measurements performed only over surface #1 produce a condition number some four orders of magnitude worse. Interesting, measuring a single component over the two levels does not produce much worse results than measuring all

components over only a single level. Measuring only the single Hz component over only a single level, today's norm, produces the worst condition number by many orders of magnitude.

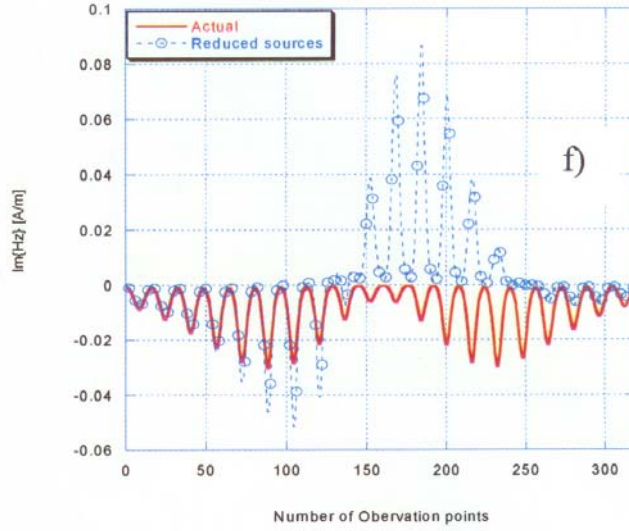
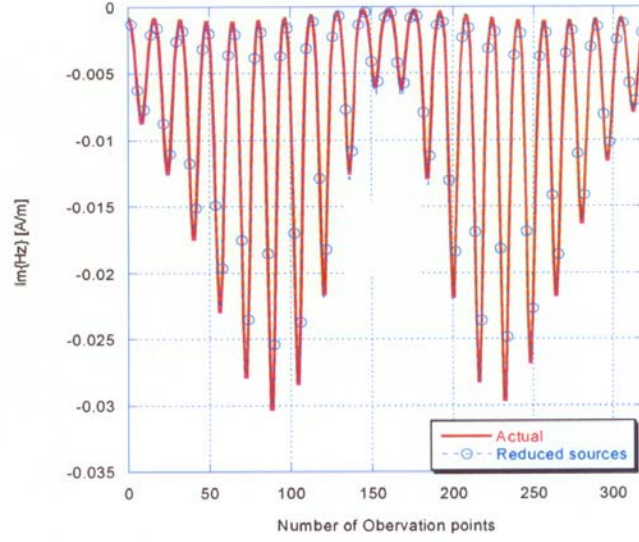


Figure 6. Top: Good agreement between "actual"  $H_z$  (here: horizontal fields) computed over the Testing Area and those obtained from the SEA using the  $S_{j,k}$  inferred from vector data over the PID surfaces. Bottom: Poor agreement for the same, using only scalar ( $H_z$ ) data on the BC surfaces to obtain the  $S_{j,k}$ .

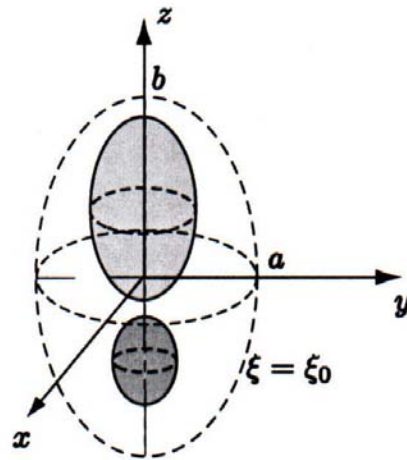


Figure 7. Synthetic compound object from which a known signal can be produced for use in the ill-conditioning evaluation.

Doubtless, the details of this rather artificial test will be altered by the particulars of any real circumstance. Further, the absolute value of the condition number in some approaches may be sufficient, although it is not as good as that for the maximum information approach. Be all this as it may, this little exercise suggests a few observations:

- In solution for SEA response coefficients, using all three vector components is likely to provide a conditioning advantage by orders of magnitude;
- Flexible positioning, including changes in sensor elevation, will also produce very substantial advantages;
- In survey strategies (measurement protocols) such as those tested, it behooves us to have positioning that is as accurate as possible, in order to minimize the error that will be amplified by any remaining ill-conditioning.

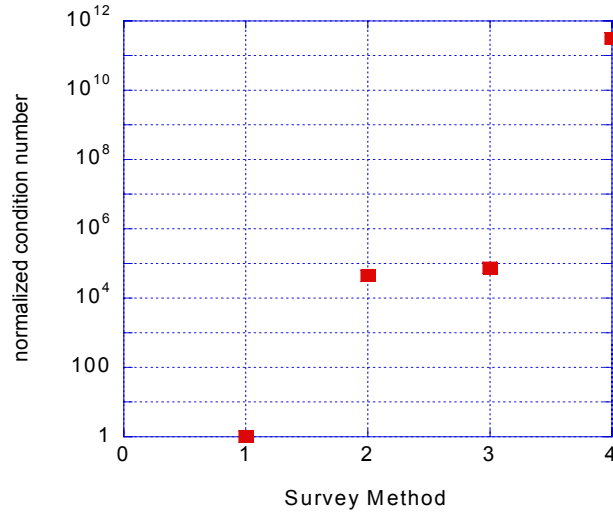


Figure 8. Condition numbers of the matrices from the four different survey methods, relative to that for the first one.

## 4. Materials and Methods

Some treatment of the material and methods, as well as the results and accomplishments, has been presented in publications in the course of the work [1,2]. While leaving some technical material out, the particulars provided here summarize and supplement those publications.

### 4.1 The GEM-3D Sensor Head

Geophex Ltd has designed and constructed the GEM-3D sensor based on its established GEM-3 device [11]. Like the GEM-3, the GEM-3D contains "horizontal" transmitter coils in the configuration shown in Figure 1, which can actually easily be oriented in any direction. To understand the method used to construct the GEM-3D, consider the schematic diagram of magnetic field lines radiating from our sensor, impinging some UXO-like object (Figure 9). Any localized source of a magnetic field will tend to produce spreading fans of field lines of the sort illustrated. In reality, these lines continue so that each one forms a closed loop, ending where it began. For simplicity we only show here the portions of the lines relevant to the sensor-target interaction. The implication of each of these lines is that at each point on the lines the magnetic

field vector is tangential to the line. Around the central cavity within the horizontal Tx coils is a horizontal Rx coil, where the counterbalanced transmitting coils nullify the primary field so that the secondary field may be apprehended. Figure 10 shows calculated primary field contours over a vertical plane above the sensor head, i.e. in a plane perpendicular to and bisecting the Tx coils.

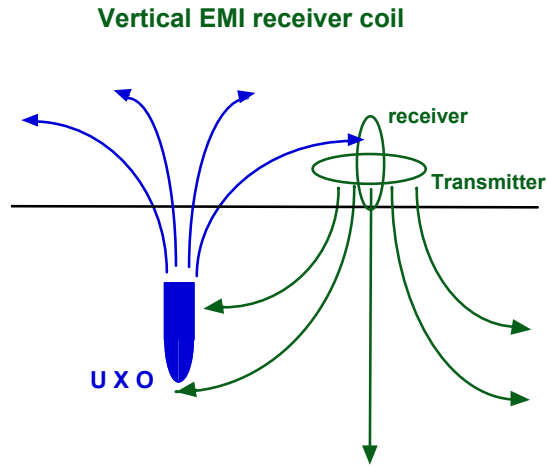


Figure 9. Schematic of GEM-3D and UXO with the magnetic field lines produced by each.

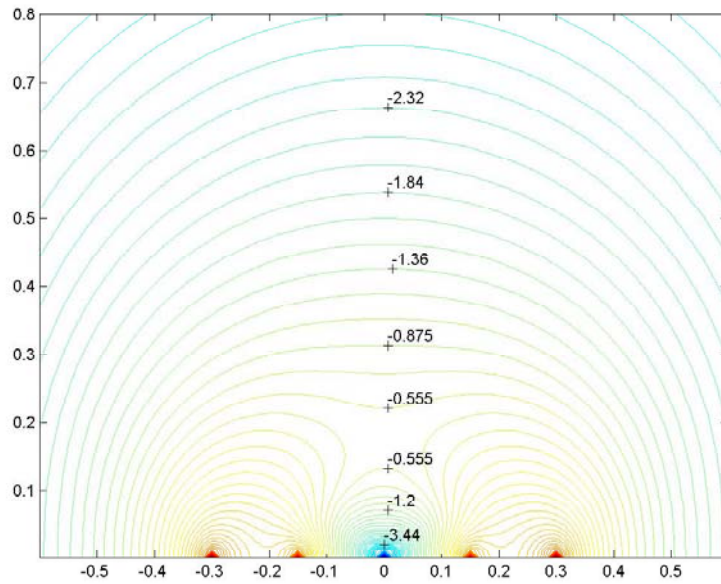


Figure 10. Contours of the logarithm of transmitted magnetic field magnitude for a GEM-3 type coil configuration. Blue = low, red = high. Horizontal axis runs across the surface of the sensor head; vertical axis is normal to it, axis units are meters. Red concentrations on the horizontal axis surround the two sets of transmitter loop wires.

How are the vertical coils be isolated from the primary field? Three things accomplish this:

1. Careful alignment of the coils perpendicular to the plane of the horizontal transmitting coils. Because each transmitting coil is circular, the “fan” of field components it produces, illustrated in Figure 9, is symmetric around the vertical axis of the coil. This means that all the field lines will be tangential to the plane of each vertical coil, and theoretically will produce no signal in it (only magnetic flux *through* the coil induces currents around the coil).
2. As much as is practical, the vertical coils will reside in the null region created by the counter-flowing transmission currents (blue region at the bottom center in Figure 10). The radii of the Rx coils is about 6 cm. Note in Figure 10 that the primary field does not grow to a substantial fraction of its maximum within that distance above the zero point.
3. Reduced by these two factors, any remaining linkage between the transmission and vertical receiving coils is calibrated out as background.

Figure 11 shows the new vector sensor head as actually constructed, with the three Rx coils. The horizontal Tx and Rx coils are encased within the rigid disk to which an extendable hand can be attached. The measured data displayed below in Section 5 attest to the success of this design.

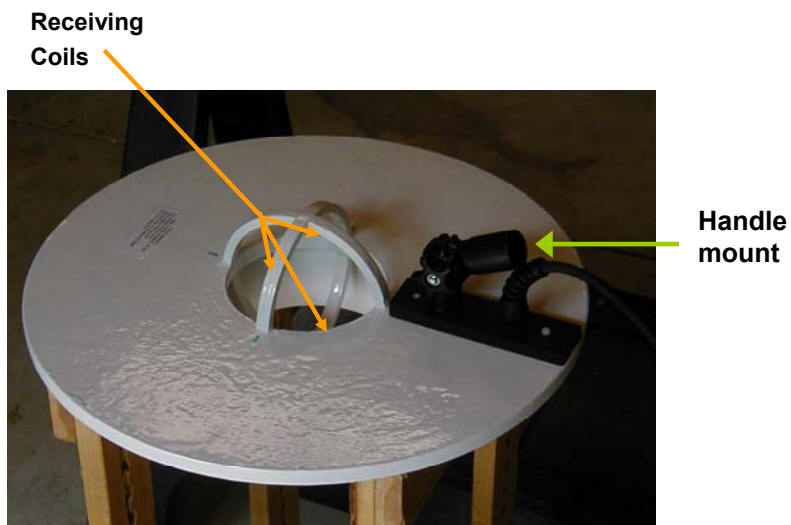


Figure 11. The GEM-3D sensor head.

## **4.2 Electrical Engineering Implementations**

A special electronics console was been built, utilizing the latest (under development) digital modules including analog-to-digital converters (A/D) with double the sampling rate (192 kHz) from the current production GEM, and smaller, low-power digital signal processors (DSP). The A/D's have a built-in anti-aliasing filter based on an over-sample and digital filter/decimation architecture. In order to accommodate the three receiver channels in the GEM-3D, two dual-channel A/D's are incorporated to digitize the three receiver coil voltages and the reference coil voltage (all three channels are normalized by the same reference). The signal processing, consists of computing the inphase and quadrature components at up to 15 frequencies continuously, relative to the Tx signal in the reference coil. This is achieved by three DSP's running off the same clock, each devoted to one receiver coil. Data are output in near real-time over three RS-232 serial ports to a laptop running a special version of WinGEM user-interface software that displays and logs the three data streams. With the new electronics design, the total package is no larger or power hungry than a standard GEM console. Three pre-amplifiers similar to the one in the standard GEM-3 are embedded in the coil disk for the three receiver coils. Another gain stage for each input resides in the console in front of the A/D channels.

Certain features in a standard GEM are not implemented in this prototype GEM-3D, including internal data storage and automatic calibration. The latter is performed now in a post-processing step utilizing measurements of ferrite and/or standard sphere targets. External 12 V power is required (battery or power supply) since there is no battery compartment built into the console.

## **4.3 Laser Positioning**

To achieve the desired positioning, we have integrated an Arcsecond laser positioning system into the GEM-3D sensor. The positioning system functions independently from the GEM-3D, and is merged through time stamping based on standard Windows OS time. Because the Arcsecond system samples at a different rate than the GEM, interpolation is used during the post-process merger, with relative local x/y/z position of the three Arcsecond sensors embedded in the GEM-3D data files for each GEM data sample. Both systems are controlled by the same laptop,

requiring a total of six serial ports accommodated with a USB to RS-232 hub. The Arcsecond positioning system comes with interface software for configuring the system and logging data.

The laser system features two eye-safe spinning laser transmitters, which are placed at reference positions somewhere near the terrain of interest (Figure 12). Redundant transmitters can be added for easier preservation of line of sight connection to the laser receivers. The distance between laser transmitters and receivers is partly a function of the power of the particular system being used, the number of transmitters, and the needs of the survey. With standoff here on the orders of  $\sim 10$ 's of meters and usually less, positional accuracy on the order of less than 1 mm is achievable. Arcsecond systems have in fact been developed to span considerably greater distances, and doing so would be an advantage in many UXO survey applications. However here we are keeping the focus on small range for the purpose of proof of concept.

The known locations of the transmitters, angles of transmissions, and timing of laser signals allows determination of the positions of three receivers attached to the EMI sensor. As long as these receivers have any known (rigid) relation to the sensor head (avoiding obviously pathological configurations e.g. linear alignment), one can determine the X,Y,Z position of the center of the sensor head as well as all tilt angles. Figure 12, right, shows an early realization of the concept. The sensor head has been blackened to minimize multi-path problems from unwanted laser reflections. Initially the tubular amplifiers were located further from the sensor head, but it was determined that closer connection to the receivers was substantially advantageous. While the presence of this positioning equipment on the sensor head itself did not disturb the GEM measurements beyond what could be calibrated out, the GEM electronics did tend to interfere with the signals from the laser receiver system. After some improvement in shielding the laser receiver plane was simply raised about 30 cm above the EM sensor head, eliminating essentially all remaining problems. The rig shown in Figure 13, in which this was all accomplished with styrofoam and duct tape, was serviceable for about forty rounds of test measurements on spheres, cylinders, various UXO's, and miscellaneous clutter. With the resolution of timing issues between the Windows-based Arcsecond software and the DOS-based GEM software, one can combine the data into files containing both position and EM data together.



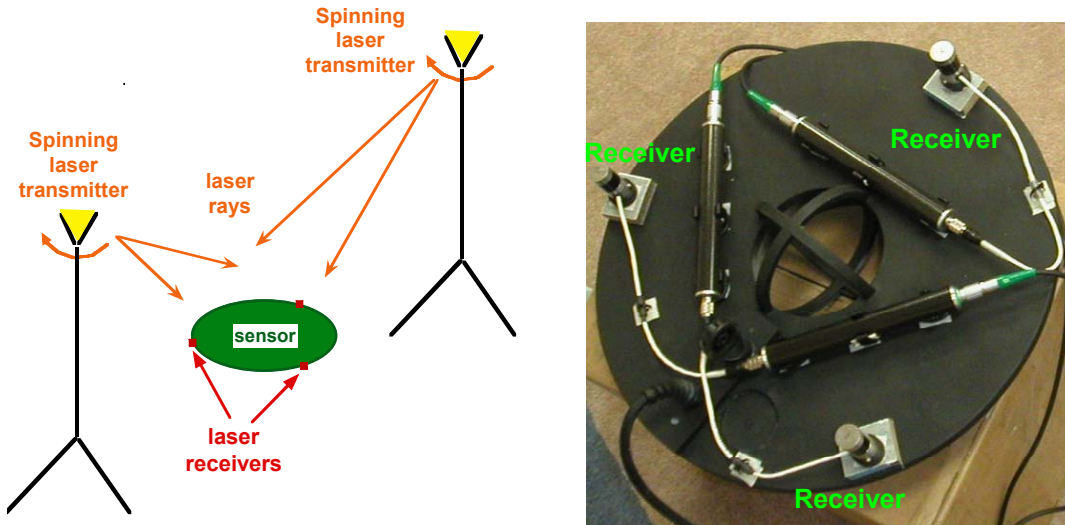


Figure 12. Left: Schematic of the laser positioning system concept, with three receivers located on the plane of the Tx coils of the EM sensor head. Right: An early realization of the system, with tube shaped amplifiers also attached to each laser receiver.

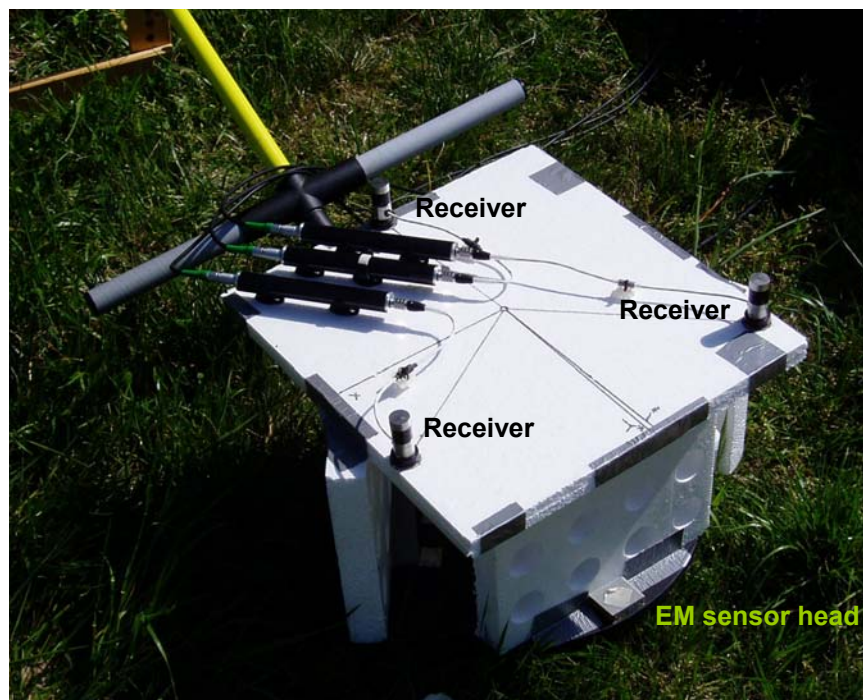


Figure 13. Most current application of the system, similar to the concept in Figure 12, right, but with the plane of laser receivers and amplifiers displaced about 30 cm above the sensor head, on styrofoam.

## 5. Results and Accomplishments

Figure 14 shows example data obtained from the GEM-3D along measurement lines on a plane above the vertical UXO shown (510 Hz, inphase component). The UXO is directly beneath the origin and measurement lines run in the X direction. The two plots shown on the center line (Y=0) show signal patterns along the entire length of the line. Note the telling sign reversals in horizontal components, when the sensor moves from one side of the UXO to the other. This is because on one side the secondary field impinges on a vertical coil from the "positive" side, while on the other side the target produces a horizontal field component that strikes the same coil on its negative side. This makes for more accurate determination of the target location and orientation and enables superior signature definition.

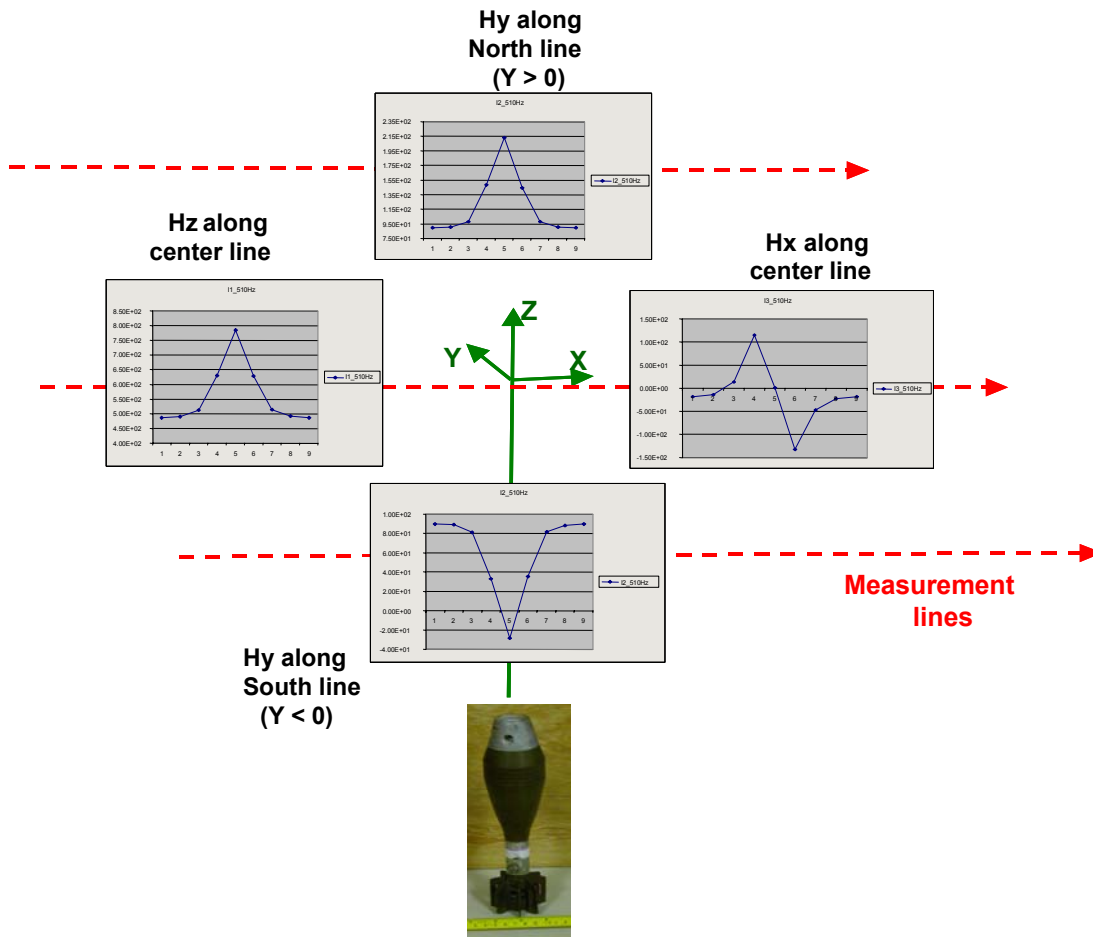


Figure 14. GEM-3D data along measurement lines in a plane over a vertical UXO.

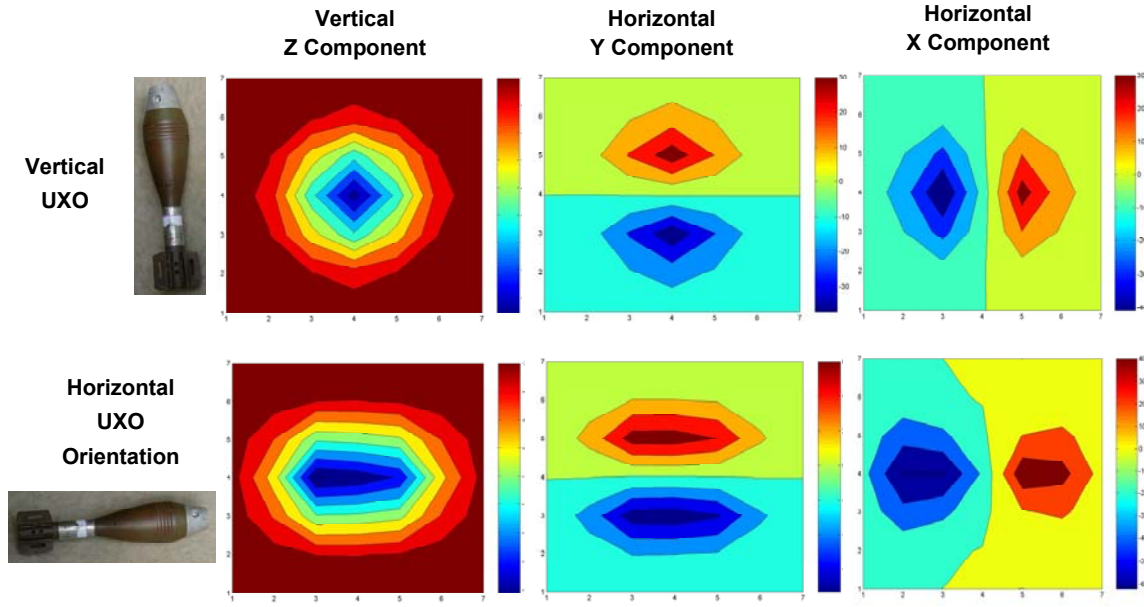


Figure 15. GEM-3D measurements at 510 Hz (quadrature component) over a plane above a UXO in vertical orientation (top row) and horizontal orientation (bottom row). The Z axis is perpendicular to the plane of the sensor head and the measurement plane. Left plots: scattered Z field component; middle,  $H_y$  component; right,  $H_x$  component, i.e. in direction aligned with the axis of the UXO when it is horizontal.

Figure 15 shows less quantitative but more detailed patterns of the 510 Hz quadrature component, over a measurement plane above the UXO. Moving the sensor through a grid of points over the target allows examination of all magnetic field components, from different views of the target, in terms of both angle of excitation and observation. The figure shows details of symmetry, asymmetry, and a distribution of signal that reflects the UXO's shape and orientation. The clear anti-symmetry of the horizontal components in the top row and the similarity of their patterns mutually rotated patterns underscore the fact that the UXO is a vertically oriented body of revolution. Otherwise either the  $H_x$  or the  $H_y$  patterns would not be symmetrical in magnitude about the center lines. When the UXO is horizontal, the secondary field distributions also reflect that fact, in the bottom row of plots. Here, because the UXO itself varies in material and geometry from one end to the other (i.e. in the X direction), we note the slight lack of magnitude symmetry in the  $H_x$  component, but not in  $H_y$ . In the least, all three components appear clearly, without distortion caused by "leakage" of the primary field.



Figure 16. Some more machined test objects to round out the prolate spheroid selection.

For more quantitative evaluation of the new system, wideband data from the GEM-3D is compared to new analytical solutions for each item in a collection of machined canonical spheroid shapes. The sensor was held at a single point above each object. The test targets include the larger items in Figure 3 and some additional steel and aluminum oblate spheroids in Figure 16. The solution system includes detailed expression of the non-uniform primary field. Comparisons for other targets are as good as those shown below in Figure 17 and Figure 18, as are those for horizontal received components, though the latter must at present be calibrated separately. Note the slight divergence of the data and analytical solutions at the highest frequencies used. Higher frequencies (beyond the range of the original GEM-3) produced greater error, evidently because of background subtraction or drift problems during the measurements. As in the case of previous GEM modifications, we expect this frequency range to be stabilized during future work.

Overall, the good agreement between the data and the analytical solutions (also developed under SERDP sponsorship) indicates that both the instrument and new solution are sound.

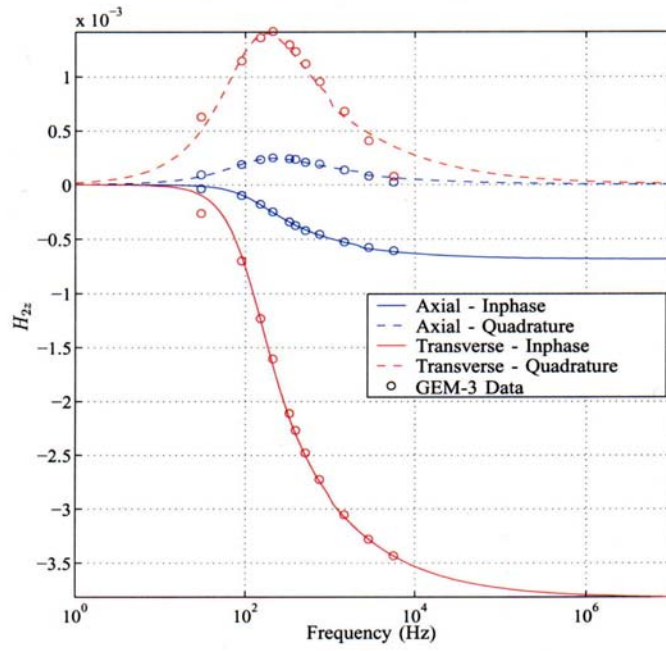


Figure 17. Comparison of GEM-3D measurements of  $H_z$  for an AL prolate spheroid.

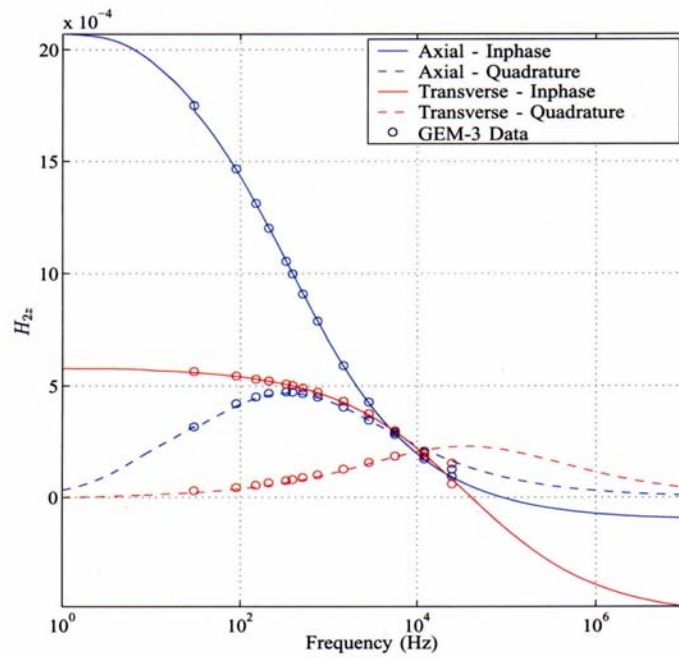


Figure 18. Comparison of GEM-3D measurements of  $H_z$  for a steel prolate spheroid.

## 6. Conclusion and Discussion:

This project set out to produce at least a bench level UWB GEM-3D EMI handheld sensor, receiving the full vector magnetic field response as opposed to only a single field component. That goal was accomplished. The device uses the established Geophex GEM-3 as its starting point, producing frequency domain output at up to 15 arbitrarily spaced frequencies in each channel, between  $\sim 30$  Hz and  $\sim 50$  kHz. Measurements with the new device compare well to analytical solutions for spheres and for canonical non-spherical shapes. Hence we believe that the instrument is working properly, producing consistent data that corresponds to interpretable electromagnetic responses from metallic targets. The addition of a laser positioning system under ERDC auspices, while still only crudely integrated, expands the utility of the device enormously. Fairly arbitrary local motion of the sensor is possible, including changes in elevation while sweeping, as well as accurately recorded tilts. The kind of data produced by this instrument or its successors in the course of close interrogation should enable a new generation of processing, inversion, and classification, such as is hinted in the motivational material presented above.

The results and implications of this project are sufficiently promising that we will submit a proposal for follow-on work in a separate document. Basically, the next logical tasks include, from specific to general, small to large:

- Stabilization of highest frequency response, and further expansion of bandwidth;
- Integration of DSP for the three channels into a single unit and software structure;
- Built in calibration, for ferrite and Q-coils, consistently across channels;
- Improvement of the laser positioning outfitting and integration: durable and rigid attachment to the sensor; better synchronization of sensor and positioning timing; portable power supplies and laptop (palmtop) control, data storage, and real time

visualization; addition of more laser transmitters to allow for more flexible motion without loss of line of sight;

- Design, development, and testing of a new generation of GEM-3D configurations aimed specifically at achieving greater range, i.e. less signal fall off with distance, possibly by stacking transmitter coils;
- Development of processing techniques and software to implement the new UXO signature recognition and inversion approaches sketched above, exploiting vector response data;
- Testing of such routines in backyard settings, for both pattern recognition as well as general inversion;
- Field testing of same at the standardized test sites and/or elsewhere.



## References

Work documented in the items in **bold blue** was supported in significant part by this project.

1. **K. O'Neill, I.J. Won, A. Oren, F. Shubitidze, K. Sun and I. Shamatava (2004). A new handheld vector EMI sensor with precise 3-D positioning, UXO/Countermining Forum 2004.**
2. **K. O'Neill, I.J. Won, A. Oren, Chi-Chih Chen, Hyoun-Sun Youn, X. Chen, and K. Sun (2004). Data diversity for UXO discrimination in realistic settings with a handheld EMI sensor, SPIE Defense & Security Symp., 12-16 April 2004, Orlando, FL.**
3. Y. Zhang, L. Collinas, H. Yu, C.E. Baum, and L. Carin (2003). Sensing of unexploded ordnance with magnetometer and induction data: Theory and signal processing, IEEE Trans. Geosci. & Rem. Sensing, vol 41, No 5, 1005-1015.
4. F. Shubitidze, K. O'Neill, S. Haider, K. Sun, and K.D. Paulsen (2002). Application of the method of auxiliary sources to the wideband electromagnetic induction problem, IEEE Trans. Geosci. & Rem. Sensing, vol 40, No 4, 928-942, 2002.
5. F. Shubitidze, K. O'Neill, K. Sun, and K.D. Paulsen (2003). Investigation of broadband electromagnetic induction scattering by highly conductive, permeable, arbitrarily shaped 3-D objects, accepted for publ., IEEE Trans. Geosci. & Rem. Sensing.
6. F. Shubitidze, K. O'Neill, K. Sun, I. Shamatava and K.D. Paulsen (2003). A hybrid full MAS and Combined MAS/TSA Algorithm for Electromagnetic Induction Sensing, accepted for publ., J. Appl. Comp. Electromagnetics Soc.
7. C.O. Ao, H. Braunisch, K. O'Neill, and J.A. Kong (2002). Quasi-magnetostatic solution for a conducting and permeable spheroid with arbitrary excitation, TGARS, Vol 40, no 4, pp.887-897.
8. B. E. Barrowes, K. O'Neill, T. M. Grzegorzczak, X. Chen and J. A. Kong (2003). Broadband electromagnetic induction solution for a conducting and permeable spheroid, submitted for publ.
9. F. Shubitidze, K. O'Neill, I. Shamatava, K. Sun and K.D. Paulsen (2004). A new numerical procedure for efficient and accurate representation of low frequency EM responses for a heterogeneous object, ACES'04.
10. **X. Chen, K. O'Neill, B. E. Barrowes, T. M. Grzegorzczak, and J. A. Kong, Application of a spheroidal mode approach with Differential Evolution in inversion of magneto-quasistatic data for UXO discrimination, submitted for publ, J. Inverse Probl.**



11. J. Won, D. A. Keiswetter, D. R. Hanson, E. Novikova and T. M. Hall, "GEM-3: a monostatic broadband electromagnetic induction sensor," Jour. Envir. Eng. Geophysics, Vol. 2, No. 1, pp53-64, 1997

## APPENDIX I

### FORWARD MODELS FOR EMI RESPONSE FOR USE IN UXO DISCRIMINATION AND SIGNAL INVERSION

Kevin O'Neill, Jan 2004

In the informal treatment that follows, I review the popular forward models for the response of UXO's or other metallic objects to electromagnetic induction (EMI) instruments, noting some of their virtues and pointing up some of their limitations. In the end, I emphasize the completeness of the modeling system recently developed within the ERDC basic and applied research program. The latter model and all the others treated are selected for discussion under the criteria that 1) for the sake of generality and range of applicability, they must have some rational physical basis or at least some strong "physical flavor" (as opposed to empirical formula fitting or straight input-output correlation); and 2) they must be fast enough and sufficiently easy to implement so that they function effectively in inversion calculations. Apologies to those whose work is not acknowledged specifically, the intent here being to summarize and critique ideas rather than to point to individual realizations. Of course, this has not impeded me from pushing my own work and that of my immediate colleagues to the fore, naming names and occasionally providing reference to documents done or in the offing. Such is the privilege of authorship of a paper on the-world-according-to-me. My hope is primarily to stimulate discussion and the exchange of ideas – and tools – amongst colleagues. Much of the essential computational and data analysis underlying results presented below was done by Dr. Fridon Shubitidze and Dr. Keli Sun of Dartmouth College. Other able contributors to concepts and some of the computations were Dr. Henning Braunisch and Dr. Chi On Ao, formerly of MIT; and Benjamin Barrowes and Xudong Chen of MIT.

#### *Single (Anisotropic) Point Dipole Model*

Perhaps the simplest and most widely used UXO EMI response model is the "point" magnetic dipole. In this idealization a UXO is represented by a possibly anisotropic point source, i.e. an infinitesimal or infinitely concentrated radiating structure. Some investigators speak of using two or three co-located ("crossed") dipoles to indicate the same thing that I mean here by a single anisotropic dipole. Expressed either way, the responding entity is located at a single point,

and responds differently to primary magnetic field components impinging upon it along different axes. While the model does possess some directional characteristics, this idealization responds *in only one way* to a given primary field component oriented in any particular direction. That is, referring to Figure 1, a primary field striking the object in either the positive or negative Z direction will provoke the same response, e.g. secondary field frequency spectrum or time history.

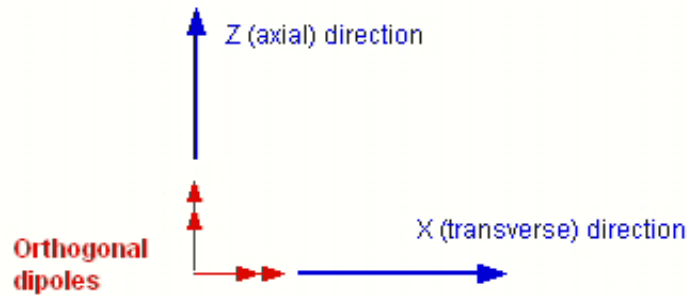


Figure 1. Crossed point dipoles, oriented in the X and Z directions.

Given that most UXO are composite objects, we performed some tests by measuring GEM-3 response of a simple construct consisting of a magnetic steel and an aluminum cylinder, one screwed into the other, represented in Figure 2 by the two-piece object between the plots. Clearly the spectra are quite different, depending on which end is up, i.e. facing the sensor. The relation between the inphase and quadrature components is quite different and the quadrature peaks are differently shaped in the two orientations, with something of a "two-lump" structure in the steel-up case. Even though the sensor is about one object length away, different parts are stimulated to differing degrees. Also, the parts closer to the sensor will register considerably stronger signals, even if they are stimulated equally.

The continuous lines in Figure 2 were produced by a detailed numerical model of the target [1-5]. As the model represents the response to the GEM-3 quite adequately, one can use it to vary distance from the object, to see whether it will respond more like a dipole if the sensor is far enough away. It doesn't. That is, the simulations reveal that one would have to be impossibly far away, by orders of magnitude, for the two axial spectra to coincide (even then, different normalizations would usually be required in the positive and negative axial directions).

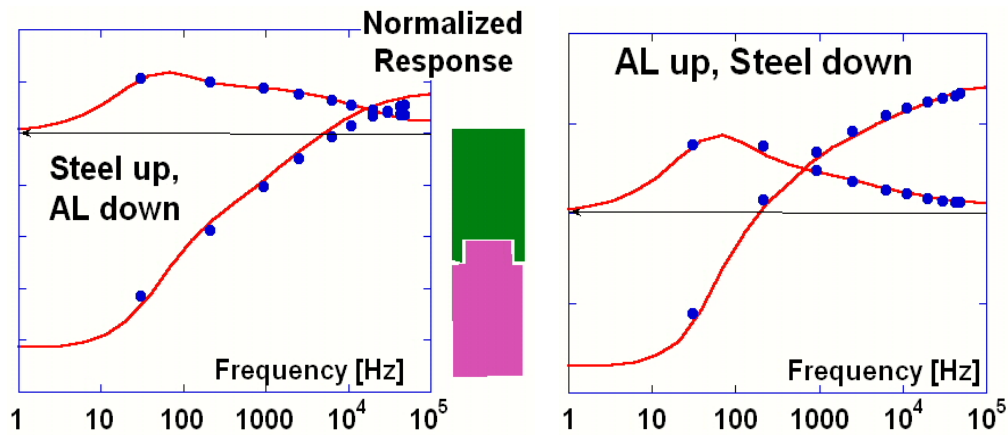


Figure 2. Response spectra for composite steel-AL target (center), measured by the GEM-3 sensor (dot markers), with the sensor head located about one object length above the target.

The implications of this effect of composite structure are far-reaching for discrimination processing and inversion. Among other things, we must recognize that, without a lot of qualification, one cannot meaningfully compare the inferred axial and transverse response of an unseen object. This is because the relation between the responses along the two axes will depend strongly on how close one is to the object and which end one is looking at in the axial view, not to mention further dependence on the frequency range or time range over which the comparison is made. Figure 3 and Figure 4 show the calculated ratio of transverse to axial response for an elongated and flattened *homogeneous* steel spheroid, respectively. Especially if one is some reasonable distance away in terms of the characteristic dimensions of the object, a quite definite pattern emerges across the spectrum. The ratio flips (relative to unity) between the low and high frequency ranges, and opposite patterns of this reversal appear for the elongated and flattened objects. Comparable effects would appear in the time domain between very early and late times. This is promising, and has been verified experimentally. However, unless steel dominates an object's response (frequently not the case), the picture becomes thoroughly muddled for composite objects. This is illustrated in Figure 5, for the case in which the AL section of the above-mentioned target is facing the sensor (right plot). The bottom line is: One cannot meaningfully work in terms of the ratio of transverse to axial response because there is no such thing as *the* axial response.

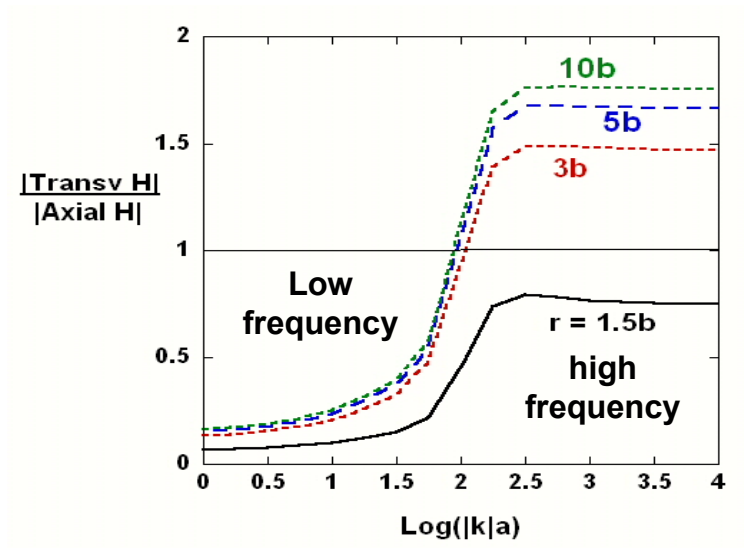


Figure 3. Calculated ratio of transverse to axial GEM-3 response by a homogeneous elongated object at different observation distances from its center ( $b$  = half length).

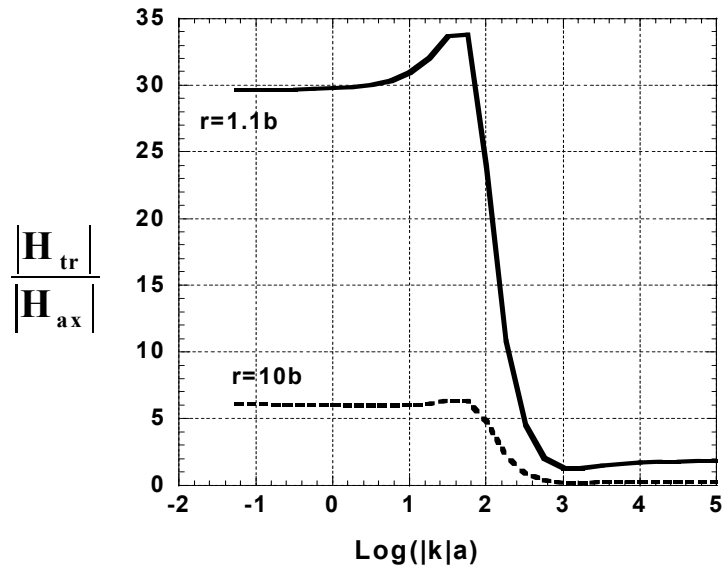


Figure 4. Same as Figure 3, but for a flattened object.

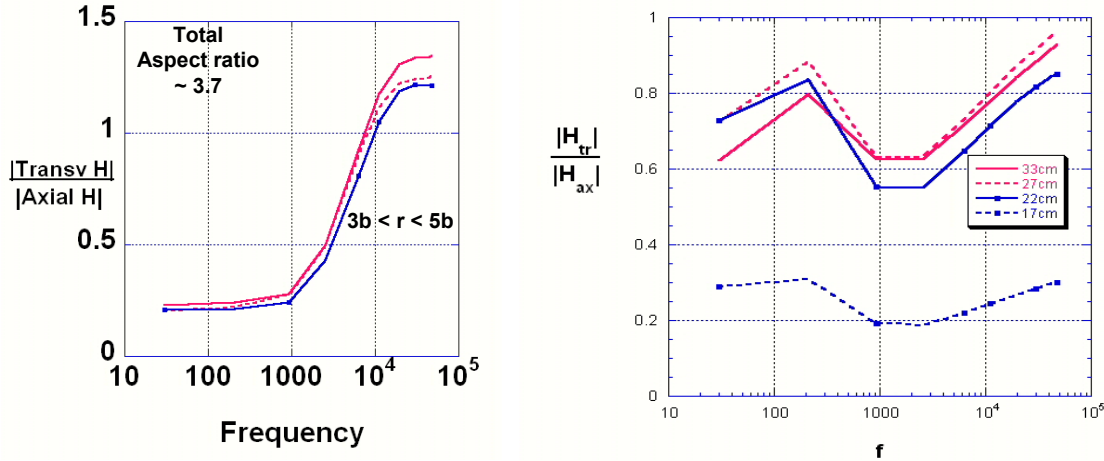


Figure 5. Measured ratio of transverse to axial responses by the composite object in Figure 2 with the GEM-3 at different distances, when the steel portion is facing the sensor (left) and when the AL section is facing the sensor (right).

### *Homogeneous Spheroid Model*

Before proceeding to more advanced dipole based models, consider another physically simple (though mathematically complex) model, namely the spheroid. Research has shown that details of surface features have little effect on EMI response, relative to the influence of overall shape and proportions of an object, e.g. [2]. This encourages us to consider spheroids to represent many objects because spheroids can assume a great variety of proportions, from flattened (oblate) to elongated (prolate) forms. The EMI spheroid solution has not been in the forefront in discrimination processing in part because, until recently, only the solution for the magnetostatic case was available. In the last few years a complete solution was developed, under SERDP auspices [6-10], including some handy simplified versions for special, problematical cases (high magnetic permeability, extreme aspect ratio). Overall, the spheroid solution reproduces the response of some irregular objects remarkably well. See frag item in Figure 6 on which the measurements in Figure 7 were made. The GEM-3 sensor head was about 10 cm from the center of the object, that being about the length of the object. Note that the item has many irregular jigs and jags in its surface, and presents a rather different profile when viewed from its broader and narrower sides. Nevertheless, its response fits that of a comparably proportioned prolate spheroid remarkably well (Figure 7). [footnote: The assumed values of  $\sigma$  and  $\mu$  are probably low. Doubling them is more realistic and produces about the same result. This non-uniqueness is fundamental, for magnetic materials, i.e. response depends inherently on the ratio  $\sigma/\mu$ , not their individual values.]

Perhaps the most remarkable thing in Figure 7 is how well the transverse analytical solution (excitation from the side) continues to resemble the frag response as the object is rotated about its long axis, presenting broader and narrower profiles to the sensor. The point to be made here is that this object is rather forgiving of a highly symmetrical mathematical idealization *because it is homogeneous in composition*. In fact, a crossed (point) dipole representation of this object would probably perform comparably well, depending a little on how far away from the object the sensor and observation point are. Overall, accumulating results suggest that when the object is homogeneous, whether flattened or elongated, the point dipole model will perform about as well as the spheroid unless 1) the primary field varies very significantly over the scale of the object, and/or 2) the observation point is closer than about half the object length.

Just as a spheroid may represent a rather irregular object pretty well, a composite object consisting of a sequence of sections could also be represented by a sequence of spheroids, end to end, each with different properties. This is done most simply, by superposition, when interaction between the sections has little effect on the scattered field, a state of affairs that is considerably more common than I would have imagined. Alternatively, new analytical solutions for multiple spheroids, including all interactions [11], could be used to model a multi-section object. However, relative to the other approaches outlined below for complex objects, the multi-spheroid approach is not recommended.

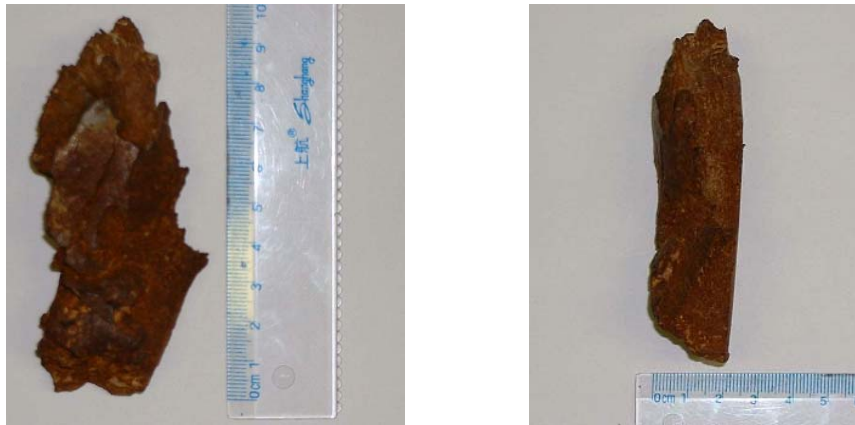


Figure 6. Piece of ordnance scrap about 10 cm in length, showing broader side (3~4 cm wide, left) and narrower side (~2cm wide, right).

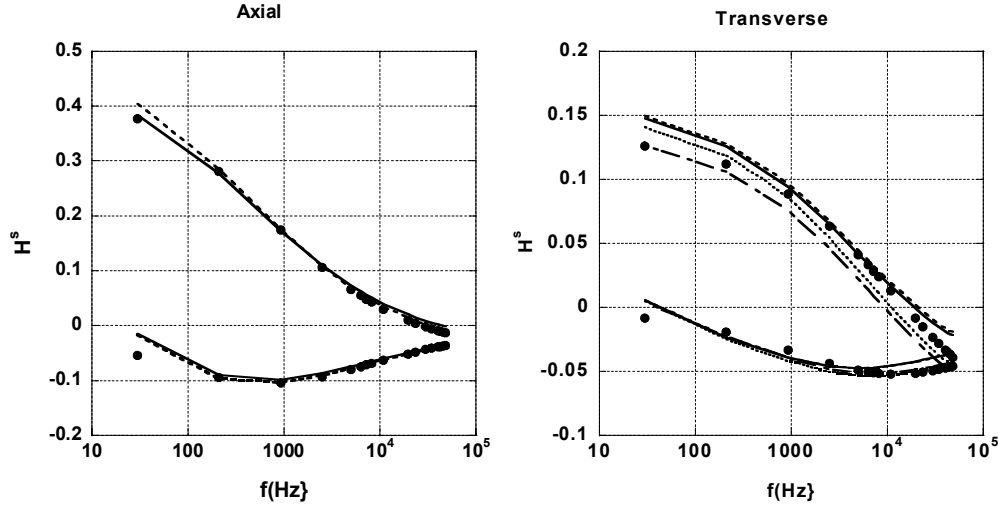


Figure 7. Comparison of the GEM-3 response from the scrap shown above (lines) with the prolate spheroid solution (dots) for semi-axis lengths  $a = 1.25\text{cm}$ ,  $b = 5\text{cm}$ , with  $\sigma = 2.6 \times 10^6 \text{ (S/m)}$ ,  $\mu = 36\mu_0$ . Different line types indicate measurements from different angles (i.e. up and down for axial case and the four principle lateral directions for transverse case). Quadrature sign convention is reversed relative to other plots.

### Multiple Offset Point Dipoles

Given that a point dipole can often represent a homogenous body pretty well, the next obvious treatment of the problem illustrated in Figure 2 is to locate a set of crossed dipoles in each section of the object [12]. This has been termed the offset or displaced dipole model, and represents a considerable improvement. Applied to the composite in Figure 2 or similar objects it will in fact succeed quite well in reproducing the EMI response, as long as one is not terribly close to the object and the primary field is not too sharply varying. A crucial point, however, is that “similar objects” must consist of clearly separable sections with particular combinations of materials such that interaction between the sections does not manifest itself significantly in the scattered field. Unfortunately, interaction frequently does have a significant effect for common material combinations and geometries. For exploration of the basis for this, see [3-4]. Here an illustration suffices. In the displaced dipole approach, one assumes that each dipole set responds specifically to the primary field striking it. That is, the set of dipoles at each point responds only to the primary field at that point, independently of the other dipole sets. Pursuing this, suppose one takes apart the two-section UXO in Figure 8 and determines the response of each section separately. The head and tail are both magnetic, but apparently consist of different metals. The



figure compares the measured GEM-3 response to that determined by the two-(displaced) dipole model and to another approach to be explained below (FXM-RSS). When the GEM-3 "looks" from the tail end of the UXO from about half an object length away, the displaced dipole solution is clearly in error (Figure 8, blue line). The picture does not improve appreciably if one moves the antenna further away, until the GEM signal fades to noise. The reason for this error resides in the interaction between the two magnetic sections. Investigations show that superposition of responses by different sections can also fail when *non*-magnetic materials are involved in certain geometries with magnetic materials. For what follows, we note that the other modeling method (green line in Figure 8) accurately accounts for all effects, and for the moment we'll use it as a standard (comparable data to be shown).

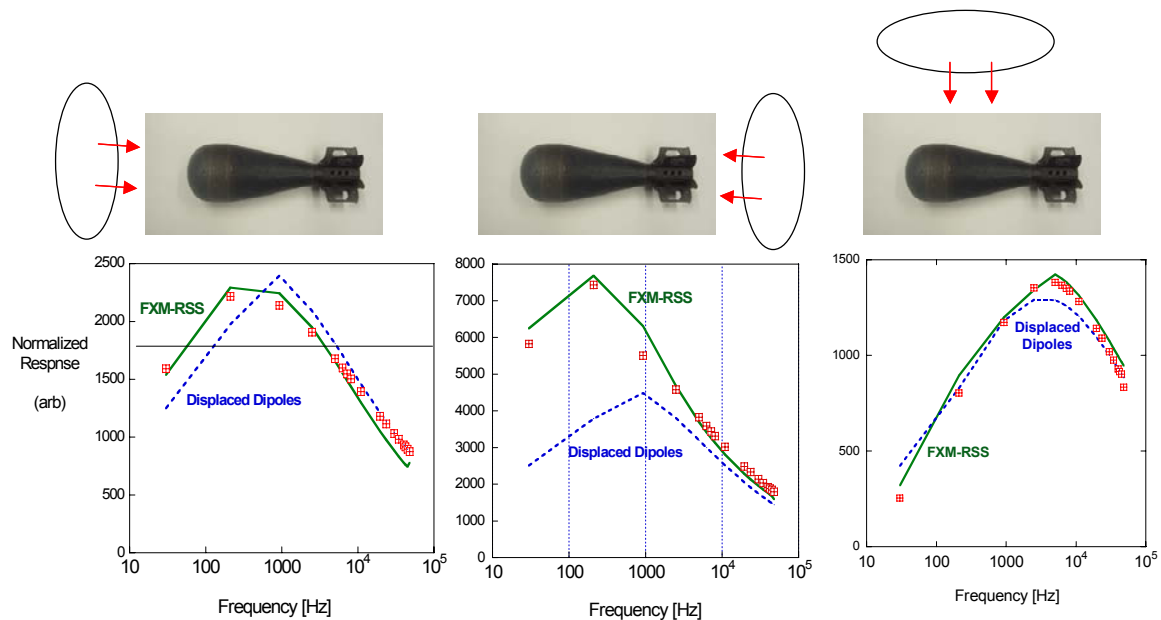


Figure 8. GEM-3 measurements (markers) compared to two modeling approaches.

During a recent Army UXO EQT program review, the question was raised: Suppose in this example you continue to let the two dipole sets respond to the primary field independently, but determine the characteristic frequency response of the two dipoles "simultaneously." That is, continue to assume that each responds only to the primary field striking it but optimally match the *combined* response of the two dipoles to the response of the *whole* object. This will help, but only superficially. This is because any movement of the antenna or object that alters the primary field will change the target's internal interactions or their significance. Thus a good match

determined for one arrangement of object and sensor will degenerate for others. For example, consider the displaced dipole response when the dipoles are solved for simultaneously, for a GEM-3 position  $D = 40$  cm from the center of the same UXO (second row in Figure 9). The match is derived from multiple data points obtained along measurement lines across each end of the target and also parallel to its axis ("horizontal" orientation). The match is pretty good. However, if one moves the antenna even 10 cm closer or farther away, the match degenerates; and a significant movement of the sensor produces very substantial error.

### *Complete Solution Using the Standardized Excitations Approach (SEA)*

Our response to this problem has been to develop a system formulated in terms of the response of the entire object, including all internal interactions, to some set of standardized excitations. In particular, we define some set of basic excitations that can be used to describe *any* primary field. The field transmitted by any of our instruments, impinging on an object in any location relative to it, is expressed as a weighted superposition of these basic excitations. At the heart of the method, one determines the response of the object to a unit magnitude primary field corresponding to each of these standard excitations. Then, for any (other) particular sensor-object configuration, the complete solution is immediately obtained just by superposition of appropriately scaled responses to the basic excitations, such as applies to the new configuration.

This is much like what has been done in radar problems for a long time. In that realm, one might determine the response of an object to a collection of unit-magnitude plane waves, each striking the object from a different angle. Any real incident beam can be constructed by some particular superposition of plane waves. The result (output, scattered field) will be the same superposition (same linear combination, same weighting) of responses to each of the constituent waves. The problem in EMI is that there are no waves. Otherwise put: There has been no immediately obvious way to express arbitrary EMI excitation fields as a sum of basic, universal, reference components. Our EMI investigations have produced ways to perform effective field decompositions in that realm. These are in many ways simpler than those for radar, possibly requiring fewer terms. In our initial investigations, the response of a target to each basic excitation mode was determined from detailed numerical modeling [1,2], including all interactions, near field effects, etc, e.g. for the results in Figure 8 and Figure 9. The same kind of thing has recently been carried out based on measurements only [13]. That is, the response of

objects to individual standard excitations has been inferred from measurements in which the primary field contained a number of these excitation components simultaneously (the normal state of affairs). Given a sufficient variety of sensor-object arrangements, one can extract the response associated with each individual excitation component. Essentially no idealization of the object or its response is required.

The first version of this approach, which we have as yet explored in the most detail, involves expressing the primary field in terms of Fundamental Excitation Modes (FXM), for lack of a better term, for the standardized excitations. In particular, these are solutions in spheroidal coordinates to the Laplace equation that governs the primary potential field. The origin is taken to be located at the target, not the sensor, and the superposition of modes expressing the primary field is valid throughout the domain. Spheroidal modes are chosen simply because spheroidal enclosing shapes and coordinate systems conform more readily to the kinds of shapes we are interested in, therefore fewer terms will be required. The primary magnetic potential field is expressed as

$$\Psi^{\text{PR}} = \sum_j b_j \Psi_j = \sum_{j=\{n,m\}} b_{mn} P_m^n(\xi) P_m^n(\eta) \begin{Bmatrix} \cos m\phi \\ \sin m\phi \end{Bmatrix} \quad (1)$$

where  $\xi$ ,  $\eta$  and the angle  $\phi$  are just the standard “radial,” “angular,” and circumferential spheroidal coordinates, respectively; the subscript  $j$  indicates all admissible combinations of  $n$  and  $m$ ; and  $P_m^n$  is the standard associated Legendre function of the first kind. These are easily calculated. The lowest modes, for each of  $m = 0$  and  $m = 1$ , correspond just to uniform (H field) axial and transverse excitation. Higher modes provide more detail for more non-uniform excitations. For a given primary field, the key is to determine the coefficients  $b_j$  that apply when the object is in any contemplated position. This also is easily done, either by integrations that exploit the orthogonality properties of the Legendre functions, or by a simple point matching scheme.

The secondary field response  $\Psi_j^s$  to the  $j^{\text{th}}$  standard excitation ( $\Psi_j$ ) is

$$\Psi_j^s = \sum_k S_{j,k} \Psi_k^s \quad (2)$$

where the  $S_{j,k}$  are coefficients scaling the basis  $\Psi_k^s$ . The latter can likewise consist of spheroidal Laplacian eigenfunctions

$$\Psi_{k=\{m,n\}}^s = Q_m^n(\xi) P_m^n(\eta) \begin{cases} \cos m\phi \\ \sin m\phi \end{cases} \quad (3)$$

where  $Q_m^n$  is the associated Legendre function of the second kind and, as for  $j$ , each value of  $k$  indicates different admissible combinations of  $m$  and  $n$ . In this case (spheroidal response modes) we write  $S_{j,k}$  as  $B_{j,k}$ . Alternatively, the  $S_{j,k}$  can represent hypothetical magnetic charge or current strengths, in which case each  $\Psi_k^s$  is the potential field produced by the  $k^{\text{th}}$  such source. In this case we write  $S_{j,k}$  as  $q_{j,k}^s$ , to distinguish the source based system from the spheroidal eigenfunction system for the scattered field. The source based system for the scattered field has the advantage that we can determine a greatly reduced source set (RSS) that produces essentially the same scattered field as a more complete, numerous set of sources. The Fundamental Excitation Mode with Reduced Source Set (FXM-RSS) is the approach with which we have the most experience to date, though the FXM-Bjk system is also under active investigation [14]. In any case, the complete secondary field can be written as

$$\Psi^s = \sum_j b_j \Psi_j^s = \sum_j b_j \sum_k S_{j,k} \Psi_k^s \quad (4)$$

Not confused yet? Then consider a last variant of the approach, which may offer numerical benefits in terms of compactness and avoidance of numerical challenges such as ill-conditioning: Each building block of the primary field,  $\Psi_j$ , can be the field produced by one (distribution of) standard magnetic sources, arrayed around the contemplated object location in a prescribed way. In this case, the coefficients  $b_j$  are primary field source (magnetic charge or magnetic current) strengths. We are actively working on this variant at present.

Despite some minor profusion of coefficients, Greek letters, indices, and alternative variants of the approach, the basic idea here is very simple:

1. In any sensor-target configuration, express the primary field as a linear combination (weighted superposition) of basic standardized excitation fields;
2. Determine the basic responses of the object, i.e. to unit magnitudes of each of these basic excitations;
3. Under any particular circumstances, obtain the complete solution by forming a linear combination of the basic responses using the same weights  $b_j$  as produced the primary excitation. That is, a given linear combination of inputs will produce the same linear combination of corresponding outputs.

In practice, we are generally solving for the  $S_{j,k}$  here. In any instance, we know (can calculate readily) the weights for the primary field,  $b_j$ . The basic building blocks of the response  $\Psi_k^s$  are just defined functions, either spheroidal Laplacian eigensolutions or fields corresponding to prescribed arrangements of unit magnitude sources. For the lowest excitation mode  $j = 0$ , the primary field is just a uniform axial H field of magnitude  $b_0$ . The corresponding response coefficients  $S_{0,k}$  are just source magnitudes or spheroidal function weights that produce the response to such a primary field. The fundamental difference between these  $S_{0,k}$  and magnetic polarizability coefficients in the single or multiple dipole models is that each of these  $S_{0,k}$  represents the response of the *entire* target, including all internal interactions. Linked to this, the secondary field expressed through these  $S_{0,k}$  (and their higher order brethren) are valid in near, middle, and far field. This is the reason for the success of the green line in Figure 8 and the blue line in Figure 9.

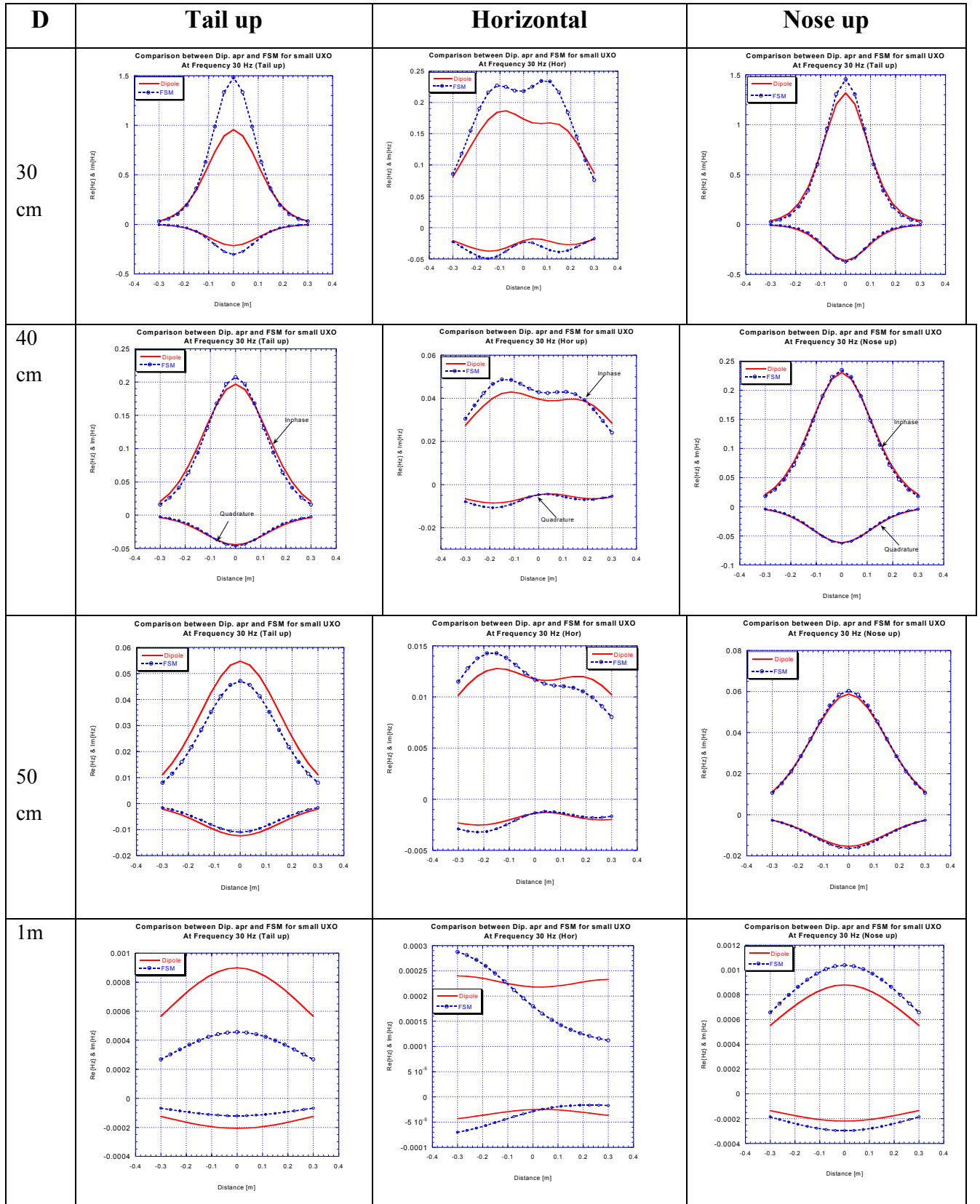
### *Concluding Discussion and Author's Opinions*

Overall, we have shown that the single dipole, multiple dipole, and homogeneous spheroid models may be adequate for some targets, under many circumstances. But we know that that will not always be the case. Many UXO exhibit the kind of heterogeneity and complexity, and many sensors produce the degree of non-uniformity in transmitted fields that tend to produce the model failures we have seen above. Because the derivation of the SEA models is relatively straightforward and the models execute very quickly, there is really no reason not to use them in inversion routines for pattern matching or "fingerprinting" approaches. How often - for what fraction of UXO's or particular UXO's - do we need the more complete SEA models? This is an object of current investigation. We have acquired EMI data sets under controlled settings for the standard set of UXO's, as well as some others. This data is being analyzed and forward models developed, specifically but not exclusively based on the SEA. In any case, the resulting SEA models for the standard target set will be distributed and should be easy to use. Interestingly, once the responses of a given UXO to the standardized inputs are determined using one instrument, it is in principle not necessary to determine them explicitly for another instrument. All that should be necessary is to construe the primary field from the new instrument in terms of the same basic excitation modes, and that is easily done. The limit on this comes when one instrument produces excitation modes that the original device does not. So far we are deriving solution for primary fields from the SAM system (uniform field), from a hypothetical point dipole source, from various size GEM-3 devices, and from the Zonge NanoTEM.

The point dipole forward models have some advantage in simplicity - but not enough to warrant their use relative to the standardized excitation approaches. Particularly for a "fingerprinting" approach to UXO discrimination, the main work in the SAE is done upfront, prior to processing. One studies UXO's of interest under controlled settings, and deduces their basic responses to each basic excitation. Once these responses are stored in either magnetic source or fundamental spheroidal mode parameters, computing the secondary field under any particular circumstances is relatively simple and very fast. In the "fingerprinting" approach, one searches through possible responses produced by the response parameters identified (stored) for each UXO type, in different locations and orientations, until the best match with observed fields is obtained. Any (as yet undetermined) difference in computing time between the different approaches for this calculation should be inconsequential.

A more general inversion approach for UXO discrimination is possible with both the earlier models and the SEA. In contrast to the “fingerprinting” approach, one would not compare measured responses to a set of catalogued possibilities, i.e. corresponding to those produced by model parameters for specific UXO types. Instead, one simply seeks any model parameters that produce fields providing an optimal match with observations. Then those parameters are examined, based on some training system or classification scheme, to determine whether the unknown object is *UXO-like* or not (elongated or flat, BOR or not, composite or homogeneous, large or small, magnetic or non-magnetic, etc). In the dipole based approach this is done in terms of the inferred dipole moments (magnetic polarizability coefficients) and, possibly, their physical separations. In the SAE this is simply done in terms of the inferred  $S_{j,k}$  coefficients, e.g. [14].

Figure 9. (below) Simultaneously determined displaced dipole response and FXM-RSS response for the UXO when the GEM-3 sensor is located different distances  $D$  away from the UXO.





## REFERENCES

1. F. Shubitidze, K. O'Neill, S. Haider, K. Sun, and K.D. Paulsen (2002). Application of the method of auxiliary sources to the wideband electromagnetic induction problem, *IEEE Trans. Geosci. Remote Sens. (TGARS)*, vol 40, No 4, 928-942, 2002.
2. F. Shubitidze, K. O'Neill, K. Sun, and K.D. Paulsen (2003). Investigation of broadband electromagnetic induction scattering by highly conductive, permeable, arbitrarily shaped 3-D objects, accepted for publ., *TGARS*.
3. F. Shubitidze, K O'Neill, K. Sun, I. Shamatava and K.D. Paulsen (2003). A hybrid full MAS and Combined MAS/TSA Algorithm for Electromagnetic Induction Sensing, accepted for publ. *J. ACES*.
4. F. Shubitidze, K O'Neill, K. Sun, and I. Shamatava (2003). Interaction between highly conducting and permeable metallic objects in the low frequency EMI range, *Proc. ACES (Applied Computational Electromagnetics Symp)*, 2003, Monterey CA, 24-28 Mar 2003, p.625-631.
5. F. Shubitidze, K O'Neill, K. Sun, I. Shamatava and K.D. Paulsen (2003). Coupling between highly conducting and permeable metallic objects in the EMI frequency range, accepted for publ., *J ACES*.
6. H. Braunisch, C.O. Ao, K. O'Neill, and J.A. Kong (2001). Magneto-quasistatic response of conducting and permeable prolate spheroid under axial excitation, *TGARS*, vol. 39, pp. 2689-2701.
7. C.O. Ao, H. Braunisch, K. O'Neill, J.A. Kong, L. Tsang, and J.T. Johnson (2001). Broadband electromagnetic induction response from conducting and permeable spheroids, *Proc. SPIE*, vol.4394: Detection and Remediation Technologies for Mines and Mine-like Targets VI, Orlando, April 16-20, 2001, p.1304-1315.
8. C.O Ao, H. Braunisch, K. O'Neill, and J.A. Kong (2002). Quasi-magnetostatic solution for a conducting and permeable spheroid with arbitrary excitation, *TGARS*, Vol 40, no 4, pp.887-897.
9. B. E. Barrowes, K. O'Neill, T. M. Grzegorzczuk and J. A. Kong (2003). Asymptotic expansions of the prolate angular spheroidal wave function for complex size parameter, submitted for publ., available on request.
10. B. E. Barrowes, K. O'Neill, T. M. Grzegorzczuk, X. Chen and J. A. Kong (2004). Broadband electromagnetic induction solution for a conducting and permeable spheroid, submitted for publ., available on request.
11. B. E. Barrowes, K. O'Neill, T. M. Grzegorzczuk and J. A. Kong (2003). Simultaneous solution for the electromagnetic induction (EMI) response from multiple conducting and permeable spheroids, to be submitted (avail. on request).

12. Y. Zhang, L. Collins, H. Yu, C.E. Baum, and L. Carin (2003). Sensing of unexploded ordnance with magnetometer and induction data: Theory and signal processing, TGARS, vol. 41(5), pp. 1005-1015.
13. K. Sun, K O'Neill, F. Shubitidze, I. Shamatava, K. D. Paulsen (2004). Fundamental Mode Approach to Forward Problem Solutions in EMI Scattering - Inferring fundamental solutions from training data, ACES'04, accepted for publ.
14. XuDong Chen, K. O'Neill, T.M. Grzegorzcyk, B.E. Barrowes, C.D. Moss, B-I Wu, J. Pacheco, and J.A. Kong (2003). Fundamental mode approach in electromagnetic induction scattering and inversion, Proc. PIERS'03, Honolulu, 13-16 Oct 2003, p318, full presentation avail. on request.